1-1-2014

Heavy Element Doping for Enhancing Thermoelectric Properties of Nanostructured Zinc Oxide

Priyanka Jood
Rensselaer Polytechnic Institute

Rutvik J. Mehta
Rensselaer Polytechnic Institute

Yanliang Zhang
Boise State University

Theo Borca-Tasciuc
Rensselaer Polytechnic Institute

Shi Xue Dou
University of Wollongong

See next page for additional authors

Authors

Priyanka Jood, Rutvik J. Mehta, Yanliang Zhang, Theo Borca-Tasciuc, Shi Xue Dou, David J. Singh, and Ganpati Ramanath

Heavy Element Doping for Enhancing Thermoelectric Properties of Nanostructured Zinc Oxide

Priyanka Jood
Department of Materials Science and Engineering
Rensselaer Polytechnic Institute
and
Institute for Superconducting and Electronic Materials
University of Wollongong

Rutvik J. Mehta
Department of Materials Science and Engineering
Rensselaer Polytechnic Institute

Yanliang Zhang
Department of Mechanical, Aerospace and Nuclear Engineering
Rensselaer Polytechnic Institute
and
Department of Mechanical and Biomedical Engineering
Boise State University

Theo Borca-Tasciuc
Department of Mechanical, Aerospace and Nuclear Engineering
Rensselaer Polytechnic Institute

Shi Xue Dou
Institute for Superconducting and Electronic Materials
University of Wollongong

David J. Singh
Materials Science and Technology Division
Oak Ridge National Laboratory

Ganpati Ramanath[§]
Department of Materials Science and Engineering
Rensselaer Polytechnic Institute

[§]Corresponding author email: Ramanath@rpi.edu

Abstract

ZnO is a high melting point high charge carrier mobility semiconductor with potential as a thermoelectric material, but its high thermal conductivity is the limiting factor for increasing the thermoelectric figure of merit *ZT*. Here, we demonstrate that doping ZnO with heavy elements can significantly enhance *ZT*. Indium doping leads to ultralow $\kappa \sim 3$ $Wm^{-1}K^{-1}$ and a high power factor $\alpha^2\sigma \sim 1.230 \times 10^{-3}$ $Wm^{-1}K^{-2}$, yielding $ZT_{1000K} \sim 0.45$ that is ~80% higher than non-nanostructured In-Zn-O alloys. Although Bi doping also yields high Seebeck coefficient of $\alpha_{300K} \sim 500$ μVK^{-1}, Bi segregation, grain growth and defect complexing are unfavorable for increasing *ZT*. Thus, besides increased impurity scattering of phonons, the concurrence of nanostructuring and charge carrier concentration control is key to *ZT* enhancement. Our results open up a new means to realize high *ZT* thermoelectric nanomaterials based on ZnO.

Keywords: Nanobulk thermoelectrics, indium doping, bismuth doping, zinc oxide, first principle transport calculations, high figure of merit ZT

Table of Contents Figure
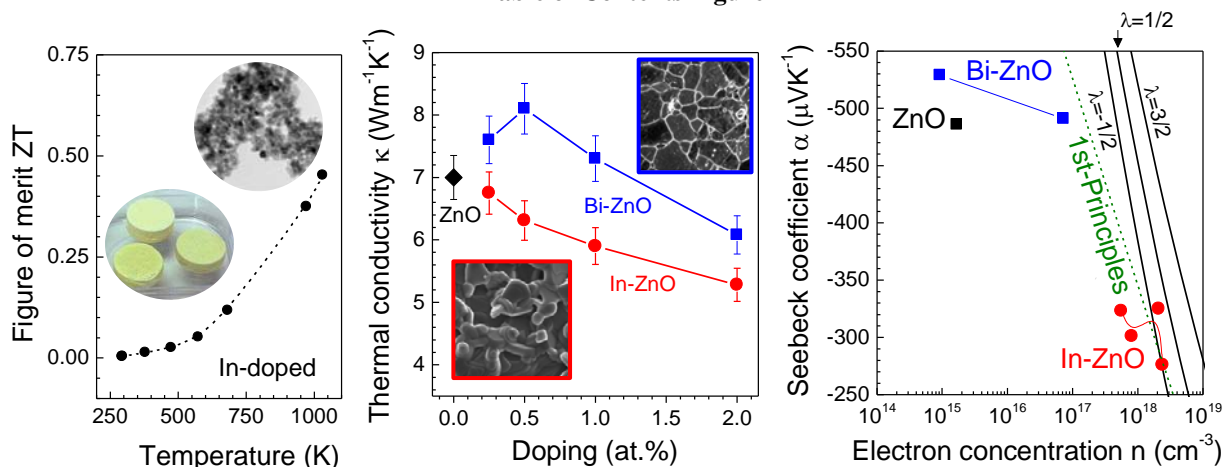
High efficiency thermoelectric devices offer great potential for harvesting waste heat into electricity[1], but require materials with thermoelectric figure of merit *ZT*>1 above 600 K. We recapitulate that *ZT* is defined as $\alpha^2\sigma/\kappa$ α is the Seebeck coefficient, σ is the electrical conductivity and κ is the thermal conductivity, and the numerator $\alpha^2\sigma$ is also known as the power factor. Zinc oxide[2] and its alloys are attractive candidates because of their high thermal stability, corrosion resistance, low-cost, and non-toxicity. But, unlike low bandgap semiconductor thermoelectrics with complex crystal structures and heavy elements, ZnO is composed of light elements and has a 3.3 eV bandgap and a relatively simple wurtzite structure. In contrast to conventional thermoelectric materials, which typically have heavy band features, n-type ZnO has a singly degenerate s-electron conduction band, with a low effective mass, $m^*=0.24m_e$, and high mobility. Thus, even though ZnO can exhibit a high Seebeck coefficient[3, 4] it does so at low carrier concentrations. In general, the Wiedemann Franz relation can be used to write $ZT = r\alpha^2/L,$ where *L* is the effective Lorentz number and $r=\kappa_e/\kappa<1$, where κ is the sum of a lattice part κ_L and an electronic part κ_e. Good thermoelectrics have sizeable values of the ratio *r* at carrier concentrations where α is also high. In ZnO, the lattice thermal conductivity is generally too high (e.g., $\kappa_L\sim\kappa\sim5$ Wm^{-1}K^{-1} at 1000 K)[5] to achieve high values of *r*. Lowering κ_L by nanostructuring combined with tapping into local strain effects, e.g., arising from the anisotropic thermal expansion[6], will be essential to realize high *ZT* in ZnO-based materials. The challenge with decreasing κ_L by nanostructuring alone is that the power factor may also decrease significantly. We have shown recently[7] that Al doping can lower κ_L by fostering grain refinement and nanoprecipitate formation while at the same time tuning the charge carrier concentration to retain a high $\alpha^2\sigma$.

Here, we report that doping ZnO with high atomic number elements can be more effective than Al for manipulating the thermoelectric properties. We show that In doping with appropriate nanostructuring of the ceramic leads to a 40% lower κ than that of non-nanostructured ZnO, while retaining a high $\alpha^2\sigma$, resulting in a *ZT* that is 80% higher than that reported for any In-doped ZnO or related alloy oxides[8], e.g., $(ZnO)_mIn_2O_3$. Our high *ZT* pellets have an exceptional fine-grained nanostructure produced *via* a microwave synthesis method. The lower κ implies that further improvements of *ZT* may be obtained by optimizing the carrier concentration by adjusting the indium content. Attempts at bismuth doping to the same level results lead to very high α and low σ implying that the bulk carrier concentration has not been effectively increased in the same way as in In-doped ZnO. We also find relatively higher κ making Bi doping unattractive for high *ZT*. Our results indicate that suitably chosen high atomic number dopants that can favorably control both nanoscale and electronic structures are attractive for realizing high *ZT* oxide-based thermoelectric materials.

We synthesized pure as well as In- and Bi-doped ZnO nanocrystals by microwaving a mixture of zinc salts with the dopant and oleylamine by adapting a scalable bottom up approach[7] (Fig. 1a-b). Transmission electron microscopy (TEM) and electron-diffraction studies confirm that each nanoparticle produced by our method is a single-crystal with the P6$_3$*mc* wurtzite structure. Nanocrystal shape and size were sensitive to both microwave dose[9] and the dopant. Microwave doses of ~50 kJ/g produce spherical ZnO nanocrystals with an average diameter d$_{avg}$ ~30 nm (see Fig. 1a),

while the introduction of $0.2 \leq$ In ≤ 2 at.% under similar conditions yields faceted nanocrystals of which many are triangular of similar dimensions for all doping levels studied (Fig. 1c). Bismuth-doped ZnO nanocrystals obtained under similar conditions are spherical (Fig. 1d) and show a size-dependence on the doping level. We obtain d_{avg} ~20 nm for ≤0.5 at.% Bi, and d_{avg} ~40 nm for 0.5 at.% ≤ Bi ≤ 1 at.%.

Optical absorption spectra from the as-synthesized In-doped ZnO nanocrystals exhibit a monotonic blue shift of E = 170 meV, implying a sharp bandgap increase with increased In doping (Fig. 1e and Fig. S1a). Comparison of our data with extant semiconductor models reveal that more than 90% of the bandgap increase is due to the Burstein-Moss effects[10,11]. In contrast, increasing Bi doping between 0.2 to 1 at.% leads to a much smaller non-monotonic blue shift of $\Delta E \sim$ 20-30 meV (Fig. 1e) attributable almost entirely to quantum confinement. These results suggest that In provides states for efficient carrier generation *via* thermal excitations, whereas Bi confines the charge carriers and does not lead to effective doping of the ZnO nanoparticles. The absence of red-shifts precludes the possibility of semiconductor-to-metal Mott transitions[12] and indicates sub-degenerate carrier concentrations $<5 \times 10^{19}$ cm^{-3}.

We fabricated 6- to 12-mm-diameter 2- to 3-mm-thick cylindrical pellets by cold-pressing the nanocrystal powder and sintering in air at 1223 K for 3 hours to ~87±3% theoretical density (Fig. 1b). X-ray diffractograms from these nanobulk ZnO pellets exhibit only Bragg reflections corresponding to the wurtzite structure with no observable second-phase peaks (supporting Fig. S1b). The increase in ZnO lattice parameters with increasing doping is consistent with unit cell volume expansion expected from the incorporation of large-radius dopants (Fig. 1f).

Indium doping refines the nanograin size, while Bi has the opposite effect. The grain size decreases nearly threefold from ~100 nm in undoped ZnO to ~35 nm for ZnO with 2 at.% In (Fig. 1g), while the same Bi doping level change increases the ZnO grain size to ~120 nm (Fig. 1h). Scanning electron microscopy (SEM) and TEM confirm both trends (Fig. 2a-c) and reveal a porosity increase for >1 at.% In doping. Bi-induced ZnO grain growth is likely fostered by accelerated mass transport facilitated by low-melting bismuth oxide formation[13] at the grain boundaries[14,15]. Grain boundary bismuth oxide formation is supported by SEM and energy dispersive X-ray spectroscopy revealing Bi-rich grain boundaries in ZnO with >0.5 at.% Bi (Fig. 2d-f). This exclusion of some Bi from the nanoparticles into the grain boundaries may be partially connected with the ineffectiveness of Bi doping in ZnO.

The room-temperature thermal conductivity κ_{300K}~7 Wm^{-1}K^{-1} for undoped nanobulk ZnO (Fig. 3a) is 7-fold lower than that of the non-nanostructured variants[5], in agreement with a modified Debye Callaway model[16,31] that accounts for nanoscale porosity and grains. Adding 2 at.% In further decreases the thermal conductivity to κ_{300K}~5.3 Wm^{-1}K^{-1}, consistent with the observed In-induced nanograin refinement. In contrast, κ_{300K} peaks at ~8 Wm^{-1}K^{-1} for 0.5 at.% Bi before decreasing to κ_{300K} ~6 Wm^{-1}K^{-1} for 2 at.% Bi. This κ increase and subsequent decrease correlate with Bi-induced grain growth, and grain boundary bismuth oxide formation, respectively. The κ values calculated by inputting nanograin and nanopore sizes measured from TEM micrographs and the nominal dopant concentration into our modified Debye Callaway model[7,31] agree well with experimentally determined κ values for both undoped and In-doped ZnO (Fig. 3a). For Bi-doped ZnO, the model underestimates κ and point to the roles of both grain boundary and impurity scattering of phonons. Grain size increase and dopant depletion due to Bi-oxide formation at grain boundaries increases κ for <0.5 at.% Bi doping. The κ decrease at higher Bi contents is attributable to the increased phonon scattering by the higher fraction of the Bi-oxide at the grain boundaries. Thus, the observed trend for Bi-doped ZnO is dependent on the interplay between competing scattering mechanisms. Almost all of κ_{300K} is accounted for by κ_L, which is consistent with the relatively low σ of ZnO.

Indium doping first increases σ by about 1000-fold from ~1 Ω^{-1}m^{-1} for undoped nanobulk ZnO to a peak σ ~10^3 Ω^{-1}m^{-1} for 0.5 at.% In, and then decreases sharply (Fig. 3c). This doping level dependence of σ can be explained by an electron concentration increase to n~4.1×10^{18} cm^{-3} at ~0.5 at.% In, followed by dopant saturation and a six-fold decrease in electron mobility μ at higher doping (Fig. 3d-e). The similar electronegativities and ionic radii facilitate In^{3+} substitution of Zn^{2+}, and are conducive for creating electron donor states that generate carriers. A similar effect[17] is responsible for a 70-fold increase in n for ≤~0.25 at.% Bi. But, further Bi addition is counterproductive (Fig. 3c-e) because of low solubility and segregation to grain boundaries as shown above, which are unfavourable for increasing either n or μ. The sharp decrease in n for >0.25 at.% Bi is likely due to the formation of defect complexes such as Bi_{Zn}-V_{Zn} or Bi_{Zn}-V_{Zn}-O_i (V=vacancy, i=interstitial) similar to P- and Sb-doped ZnO[18,19]. Defect complexing and Bi segregation to the grain boundaries[20,21] are consistent with the lack of Burstein-Moss effects in Bi-doped ZnO, as described earlier above.

Our nanobulk ZnO pellets doped with either In or Bi exhibit large negative α_{300K} due to a combination of a sub-degenerate n<10^{19} cm^{-3} doping level and nanostructuring[22, 23] (Fig. 3b). In-doped nanobulk ZnO pellets show -250 $\leq \alpha_{300K} \leq$ -325 μVK^{-1} with a maximum at 0.25 at.% In, while Bi doping yields -480 $\leq \alpha_{300K} \leq$ -530 μVK^{-1}. These α_{300K} values are 10-50% higher than reported for any standard thermoelectric samples of ZnO[5,24,25]. Uniquely, 0.5 at.% In doping yields a higher α_{300K} than the non-nanostructured counterparts at comparably high n and σ. The resultant power factor $\alpha^2\sigma_{300K}\sim 0.8\times10^{-4}$ W/mK^2 is comparable to, or greater than, that reported for any ZnO-based material[5,24,25] that simultaneously shows a low κ_{300K}.

In order to further understand the α increase, we calculated α using the Boltzmann transport equation in the relaxation time approximation using a single parabolic band model[7]. As expected for our sub-degenerate n<10^{20} cm^{-3} the experimental values deviate considerably from the calculated ionized impurity scattering dominant Seebeck coefficient curve (supporting Fig. S2a). For both dopants, the calculated curve for electron scattering by optical phonons is closest to the experimental data for $10^{18} \leq$ n $\leq 10^{20}$ cm^{-3}, as in layered ZnO$_m$In$_2$O$_3$[26, 27]. For n $\leq 10^{18}$ cm^{-3}, the calculated curve exceeds the experimental values, pointing to scattering from extended defects such as grain boundaries[28]. We also carried out first principles calculations using the actual band structure and the constant scattering time approximation[29, 30] We used a method similar to that reported elsewhere[6] but we adjusted the band gap to the experimental value in order to avoid any errors due to bipolar effects at very low carrier concentrations. Our results show that high Seebeck coefficient is possible at low carrier concentrations (see supplementary Fig. S2), as expected for high bandgap materials. Specifically, we obtain α_{300K}=-300 μVK^{-1} for n=1.9x10^{18} cm^{-3} and -500 μVK^{-1} for n=1.6x10^{17} cm^{-3}, indicating an order of magnitude difference in effective doping level for our In- and Bi-doped samples, consistent with other measurements.

Since 0.5 at.% In doping produces the best properties at 300 K, we measured the temperature-dependent properties for this composition. Increasing the temperature increases α to a maximum of -301 μVK^{-1} at 750 K before it decreases slightly to -293 μVK^{-1} at 1000 K (Fig. 4a). The 300 K Seebeck coefficient indicates a room temperature carrier concentration of n=2.5x10^{18} cm^{-3} according to our first principles calculations. The κ decreases monotonically with increasing temperature, and yields $\kappa_{1000K}\sim$ 3 Wm^{-1}K^{-1} (Fig. 4b and Fig. S3a), which is the lowest κ_{1000K} for ZnO-based materials[5,24,25]. The agreement between experimentally measured κ values and those calculated by our modified Debye Callaway model (Fig. 4b) described earlier, highlights the importance of nanostructuring for realizing ultralow κ. The monotonic σ increase with temperature to σ_{1000K} = 1.4×10^4 Ω^{-1}m^{-1} is indicative of carrier excitation by dopant ionization (see Fig. 4a and supporting Fig. S3b). This result is consistent with a roughly linear temperature-dependence of α expected for a near-parabolic-band large band gap material such as ZnO, as confirmed by our first principles calculations for a fixed carrier concentration (Fig. S2b). As a consequence of the increasing carrier concentration with temperature, we obtain a remarkably high $\alpha^2\sigma_{1000K}\sim$1230 μWm^{-1}K^{-2} (Fig. 4b) which is amongst the highest power factors reported for ZnO alloys. This combined with ultralow κ_{1000K} yields $ZT_{1000K}\sim$ 0.45 (Fig. 4c), which is ~80% higher than any ZT reported for In-alloyed ZnO, and amongst the highest for ZnO-based materials. Based on the analysis of Ong et al[6], we note that the carrier concentration is probably not fully optimized. In particular, values of n>2x10^{19} cm^{-3} at 1000 K, with somewhat lower Seebeck coefficients and higher conductivity may yield still higher ZT provided that the beneficial effects of In-doping on the nanostructure and thermal conductivity are maintained on that regime.

In summary, we have shown that suitably chosen high atomic number dopants can be attractive for favorably altering the Seebeck coefficient, and electrical and thermal conductivities, of nanobulk ZnO pellets prepared by sintering microwave-synthesized nanocrystals. In particular, 0.5 at.% In-doped shows $ZT\sim$0.45 at 1000 K, the highest reported for ZnO. Indium doping affords control of non-degenerate carrier concentrations to increase the power factor by a factor of 15 and results in ultralow thermal conductivity by inducing nanograin refinement. Bismuth doping yields Seebeck coefficients that are 50% higher than previously reported, but low electrical conductivity and high thermal conductivity due defect complex formation and grain growth, respectively.

Acknowledgements

Experimental details

Nanocrystal synthesis: In a typical synthesis, 3 g of zinc acetate (99.99% purity) and 500 µl of oleylamine ($CH_3(CH_2)_7CH=CH(CH_2)_8NH_2$) were added to 10 ml of 1,5-pentanediol (95% purity) and sonicated for 5 minutes. For preparing doped ZnO, we added either bismuth acetate (99.99%) or indium chloride (99.99%) to the solution. The mixture was exposed to 2.45 GHz microwave exposures in either a CEM Discover instrument or an off-the-shelf 1000 W Panasonic instrument. A series of experiments revealed that to obtain ZnO nanocrystals with a narrow size distribution a minimum microwave dose of 16 kJ/g is required. Thereafter the same conditions were utilized for all the syntheses. As prepared ZnO without doping was milky white whereas In- and Bi-doped ZnO suspensions were light blue or yellow colored respectively. The nanoparticles were extracted by centrifugation and sonication in alcohols and dried in a fume hood overnight.

Bulk-nanostructured pellet fabrication: The dried nanocrystal powders were cold-pressed under a load of 8 metric tons into cylindrical pellets of 6- to 12 mm diameter disks of 2-3 mm thickness. The pellets were sintered in air by heating to 1223 K at 3 K/min and holding for 3 hours. The pellets were then cooled at a rate of 4 K/min.

Materials characterization: The as-synthesized nanocrystals and sintered pellets were characterized by X-ray diffraction using a Bruker D-8 instrument with Cu Kα radiation, scanning and transmission electron microscopy, and diffraction. The nanocrystal morphology and structure and sintered pellet nanostructure was determined using a field-emission Zeiss Supra 55 SEM operated at 1-5 kV, a Philips CM 12 TEM operated at 120 kV, and a JEOL 2010 TEM operated at 200 kV. Optical spectroscopy was performed using a Cary 6000i UV-VIS-NIR spectrophotometer.

Thermoelectric measurements: Room-temperature electrical conductivity and Hall measurements on the sintered pellets were carried out using the Van der Pauw four point probe technique. A steady state technique reported elsewhere[7, 31] was used to simultaneously measure the room-temperature thermal conductivity and the Seebeck coefficient of the sintered samples. High temperature measurements of the Seebeck coefficient and electrical conductivity were made by the static DC method (ULVAC ZEM-3, USA). For temperature dependent thermal conductivity measurements we separately measured the heat capacity, the thermal diffusivity (see supporting Fig. S2) using the laser flash method with a LINSEIS Model LFA 1000 instrument, and the density of the sintered samples by the Archimedes method. Since density variation with temperature is expected to be insignificant, the room temperature density was assumed for all our calculations. The sintered thin disk-shaped nanobulk pellets were coated with graphite to ensure efficient absorption and radiation by the surface and we corrected for losses due to radiation and the finite time-interval of the laser pulse. Our error analyses for the instrumental measurement uncertainties yield the following values: ±2% for thermal diffusivity, ±10% for specific heat, ±12% for thermal conductivity, ±2% for electrical conductivity, ±2% for Seebeck coefficient and ±12% for the *ZT*[31].
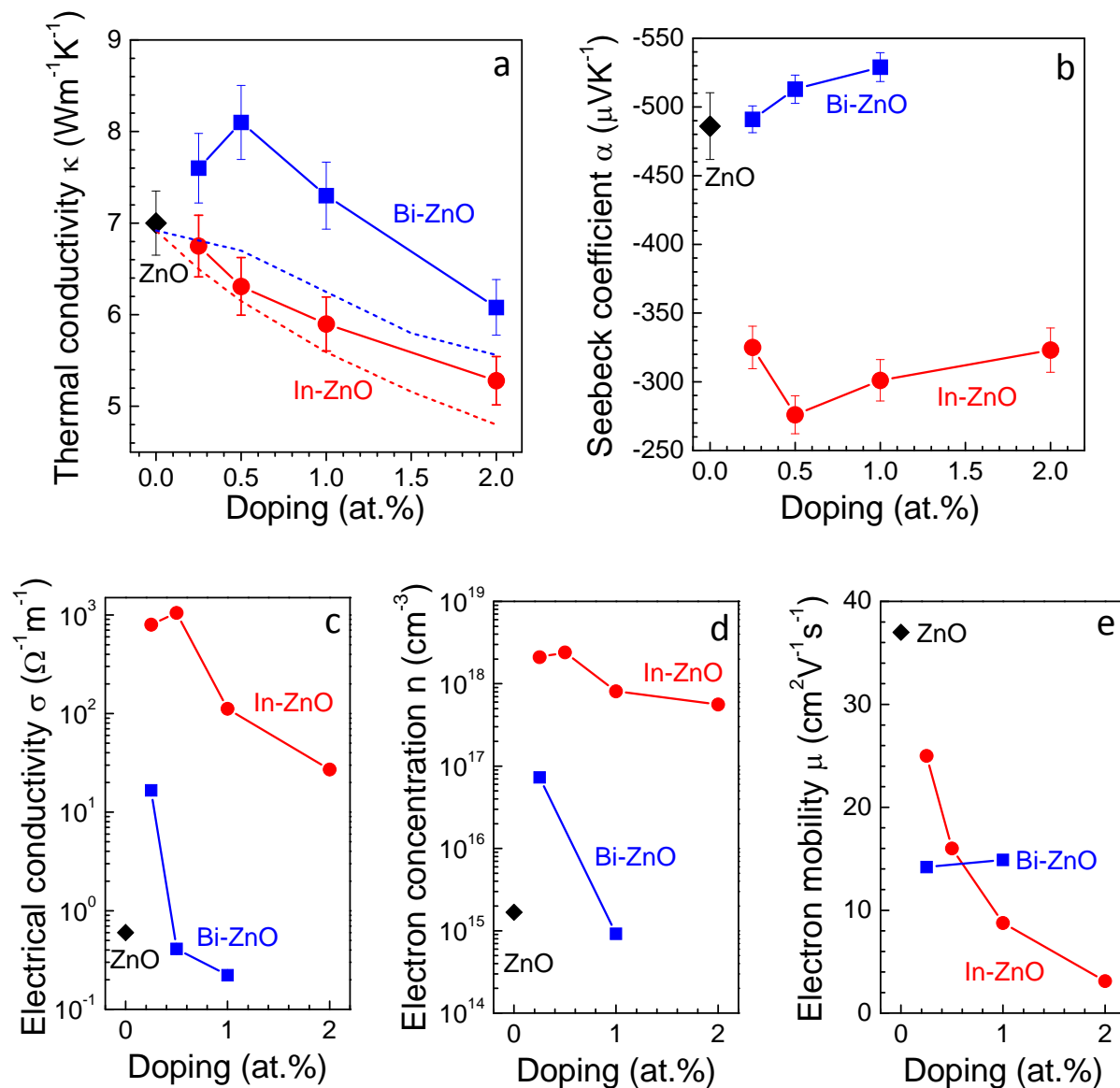
Figures
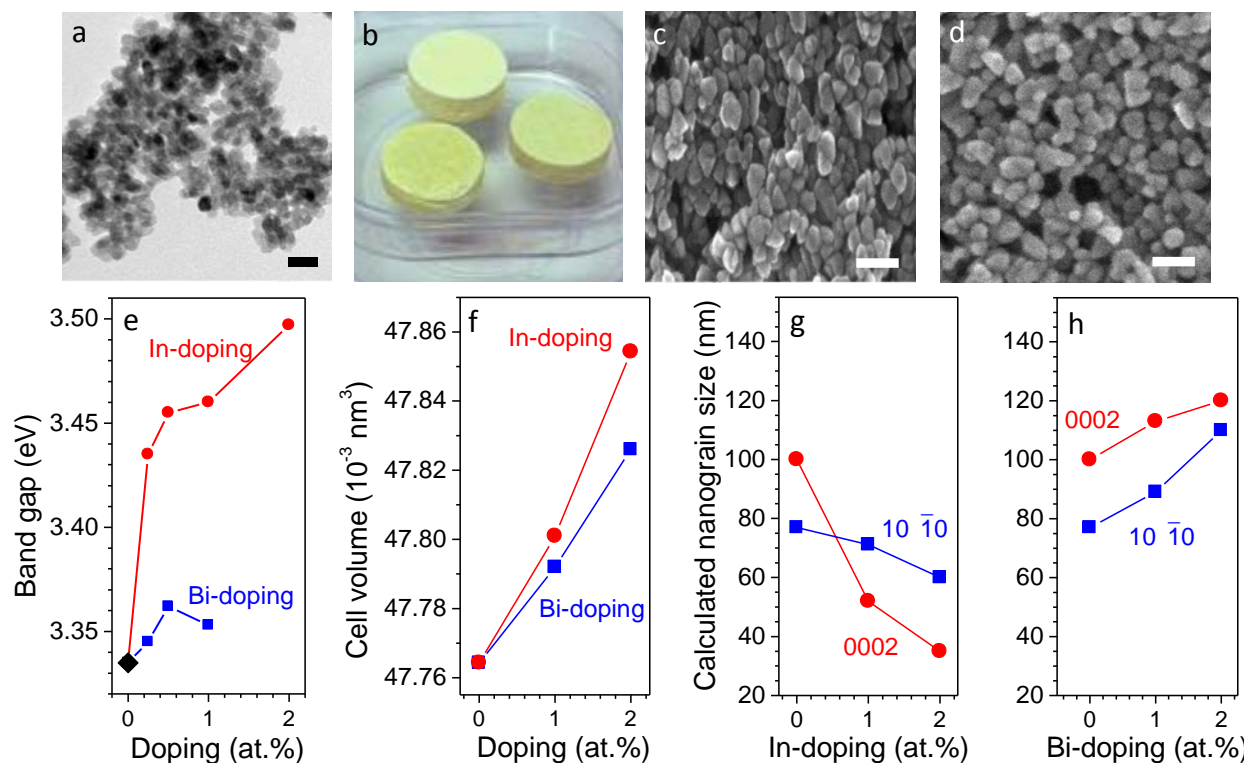
Figure 1. (a) Bright-field transmission electron micrograph showing undoped ZnO nanocrystals (b) Optical image of ½ inch diameter nanobulk ZnO pellets. Scanning electron micrographs from nanobulk ZnO pellets with (c) 1 at.% In doping and (d) 0.5 at.% Bi doping. Scale bars are 20 nm, 30 nm and 50 nm in (a), (c) and (d), respectively. (e) Optical bandgap and (f) ZnO unit cell volume of nanobulk ZnO, and (g-h) nanograin size, shown as a function of doping level. The Bragg reflections used to estimate the grain size using the Scherrer formula are also shown.
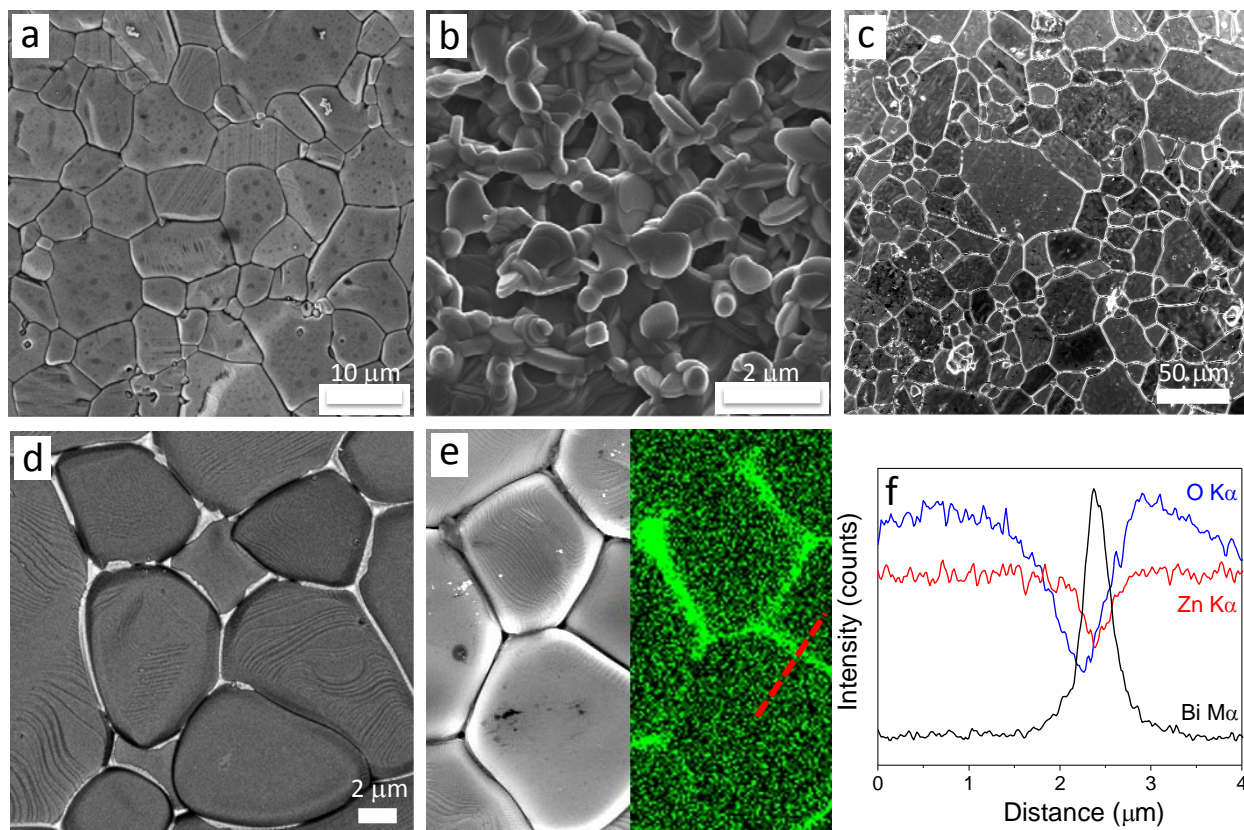
Figure 2. Scanning electron micrographs from nanostructured ZnO pellets with (a) no doping (b) 1 at.% In doping, and (c) 1 at.% Bi doping. (d) Back-scattered electron micrographs and (e) elemental map of Bi obtained by EDX shown together with a reference secondary electron image from ZnO doped with 1 at.% Bi, showing Bi segregation to grain boundaries. (d) Representative EDX line scans of O Kα_1, Zn Kα_1 and Bi Mα_1 X-rays obtained across the grain boundary indicated by the dashed red line in (e).

Figure 3. (a) Thermal conductivity κ, (b) Seebeck coefficient α, (c) electrical conductivity σ, (d) electron concentration n, and (e) Hall mobility μ, of nanobulk ZnO pellets at 300 K plotted as a function of In or Bi doping. The red circles represent In-doped ZnO, the blue squares represent Bi-doped ZnO and the black diamonds represent undoped ZnO nanobulk pellets. The dashed lines in (a) represent the modified Debye Callaway model for In-doped ZnO (lower curve, red) and Bi-doped (upper curve, blue). The solid lines joining the data points the figures a-e are only to guide the eye.
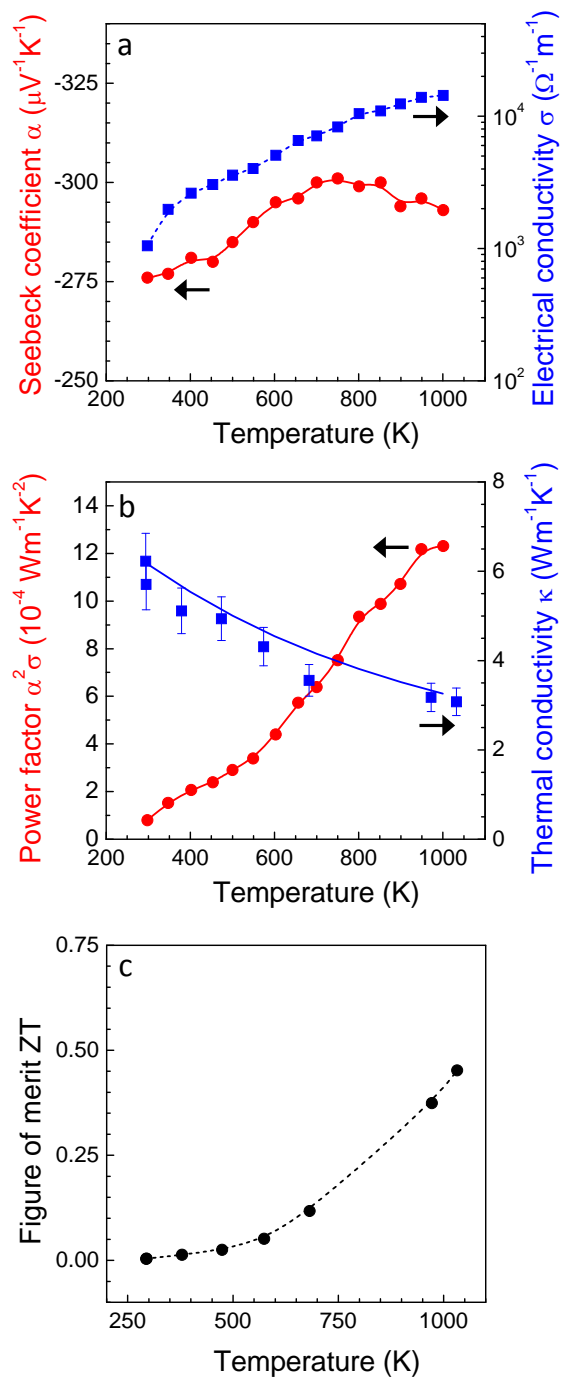
Figure 4. (a) Seebeck coefficient α and electrical conductivity σ, (b) power factor $\alpha^2\sigma$ and thermal conductivity κ, and (c) *ZT,* for nanobulk ZnO pellets with 0.5 at.% In doping. The solid blue line in (b) represents the modified Debye Callaway model.

References

1. T. M. Tritt, M. A. Subramanian, *MRS Bulletin* **2006**, 31, 188.
2. U. Ozgur, Y. I. Alivov, C. Liu, A. Teke, M. A. Reshchikov, S. Dogan, V. Avrutin, S. J. Cho, H. Morkoc, *J. Appl. Phys.* **2005**, 98, 041301.
3. M. Ohtaki, K. Araki, K. Yamamoto, *J. Electron. Mater.* **2009**, 38, 1234
4. A. F. Kohan, G. Ceder, D. Morgan, CGVd Walle, *Phys. Rev. B* **2000**, 61, 15019.
5. T. Tsubota, M. Ohtaki, K. Eguchi, H. Arai, *J. Mater. Chem.* **1997**, 7, 85.
6. K. P. Ong, D. J. Singh, P. Wu, *Phys. Rev. B.* **2011**, 83, 115110.
7. P. Jood, R. J. Mehta, Y. Zhang, G. Peleckis, X. Wang, R. W. Siegel, T. Borca-Tasciuc, S. X. Dou, G. Ramanath, *Nano Lett.* **2011**, 11, 4337.
8. H. Ohta, W. S. Seo, K. Koumoto, *J. Am. Ceram. Soc.* **1996**, 79, 2193.
9. I. Bilecka, P. Elser, M. Niederberger, *ACS Nano* **2009**, 3, 467.
10. B. E. Sernelius, K. F. Berggren, Z. C. Jin, I. Hamberg, C. G. Granqvist, *Phys. Rev. B.* **1988**, 37, 10244.
11. S. Cho, J. Ma, Y. Kim, Y. Sun, G. K. L. Wong, Ketterson JB, *Appl. Phys. Lett.* **1999**, 75, 2761.
12. K. J. Kim and Y.R. Park, *Appl. Phys. Lett.* **2001**, 78, 475.
13. J. Kim, T. Kimura, T. Yamaguchi, *J. Am. Ceram. Soc.* **1989**, 72, 1541.
14. H. Wang, Y-M Chiang, *J. Am. Ceram. Soc.* **1998**, 81, 89.
15. D. R. Clarke, *J. Appl. Phys.* **1979**, 50, 6829.
16. Y. Kinemuchi, H. Nakano, M. Mikami, K. Kobayashi, K. Watari, Y. Hotta, *J. Appl. Phys.* **2010**, 108, 053721.
17. C. Xu, J. Chun, D. E. Kim, J-J Kim, B. Chon, T. Joo, *Appl. Phys. Lett.* **2007**, 90, 083113.
18. V. Vaithianathan, B. T. Lee, S. S. Kim, *Phys. Status Solidi A* **2004**, 86, 151917.
19. T. M. Borseth, J. S. Christensen, K. Maknys, A. Hallen, B. G. Svensson, A. Y. Kuznetsov, *Superlattices Microstruct.* **2005**, 38, 464.
20. J. M. Carlsson, B. Hellsing, H. S. Domingos, P. D. Bristowe, *Surf. Sci.* **2003**, 532-535, 351.
21. V. Bhosle, A. Tiwari, J. Narayan, *Appl. Phys. Lett.* **2006**, 88, 032106.
22. M. S. Dresselhaus, G. Chen, M. Y. Tang, R. G. Yang, H. Lee, D. Z. Wang, Z. F. Ren, J. P. Fleurial, P. Gogna, *Adv. Mater.* **2007**, 19, 1043.
23. B. Poudel, Q. Hao, Y. Ma, Y. Lan, A. Minnich, B. Yu, X. Yan, D. Wang, A. Muto, D. Vashaee, X. Chen, J. Liu, M. S. Dresselhaus, G. Chen, Z. Ren, *Science* **2008**, 320, 634.
24. Y. Orikasa, N. Hayashi, S. Muranaka, *J. Appl. Phys.* **2008**, 103, 113703.
25. K. H. Kim, S. H. Shim, K. B. Shim, K. Niihara, J. Hojo, *J. Am. Ceram. Soc.* **2005**, 88, 628.
26. Y. Orikasa, N. Hayashi, S. Mauranaka, *J. Appl. Phys.* **2008**, 103, 113703.
27. C. Marcel, N. Naghavi, G. Couturier, J. Salardenne, J. M. Tarascon, *J. Appl. Phys.* **2002**, 91, 4291.
28. E. Shanthi, V. Dutta, A. Banerjee, K. L. Chopra, *J. Appl. Phys.* **1980**, 51, 2643.
29. D. Parker, D. J. Singh, *Phys. Rev. X.* **2011**, 1, 021005.
30. G. K. H. Madsen, D. J. Singh, *Comput. Phys. Commun.* **2006**, 175, 67.
31. R. J. Mehta, Y. L. Zhang, C. Karthik, B. Singh, R. W. Siegel, T. Borca-Tasciuc, G. Ramanath, *Nature Mater.* **2012,** 11, 233.
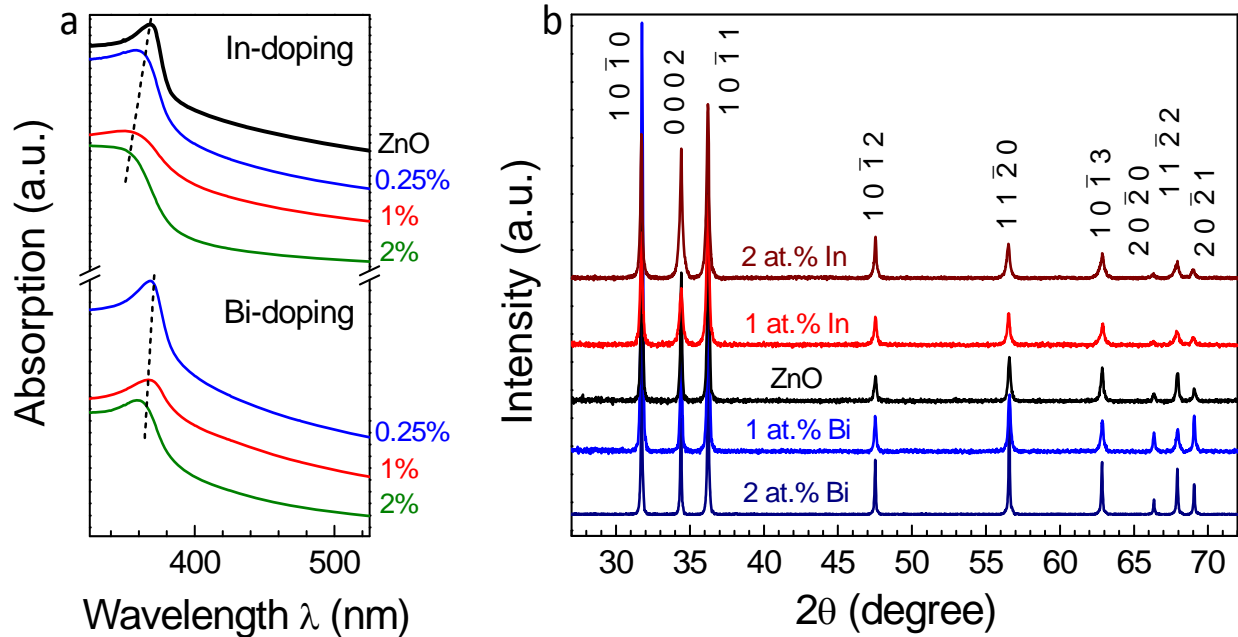
Supporting information

Fig. S1. (a) Optical absorption spectra from as-synthesized In- and Bi-doped ZnO nanocrystal solutions showing absorption band edge shifts as a function of the doping level. (b) X-ray diffractograms from In- and Bi-doped ZnO nanobulk pellets.
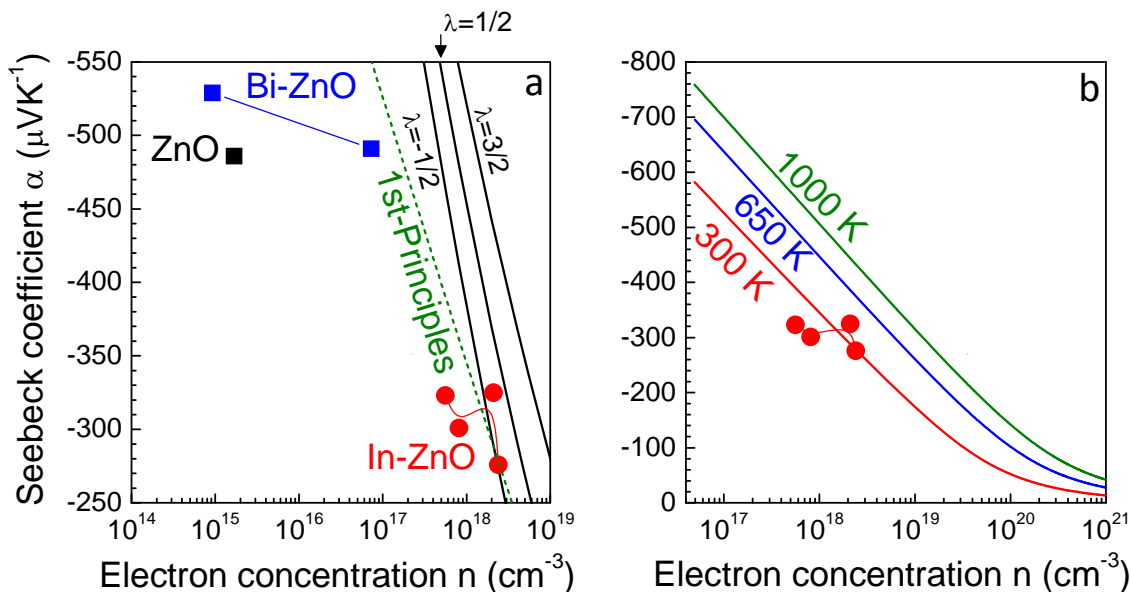
Fig. S2. (a) Room-temperature Seebeck coefficient α_{300K} plotted as a function of electron concentration. The solid lines correspond to model fits with $\lambda = \frac{1}{2}$, $\frac{3}{2}$ and $-\frac{1}{2}$, denoting electron scattering from optical phonons, ionized impurities, and acoustic phonons, respectively and the green dashed line represents the first principles model[R1]. (b) Direction-averaged Seebeck coefficient as a function of doping at different temperatures from first principles calculations carried out within the constant scattering time approximation[R1]. The red circles are experimental data from In-doped ZnO at 300 K.

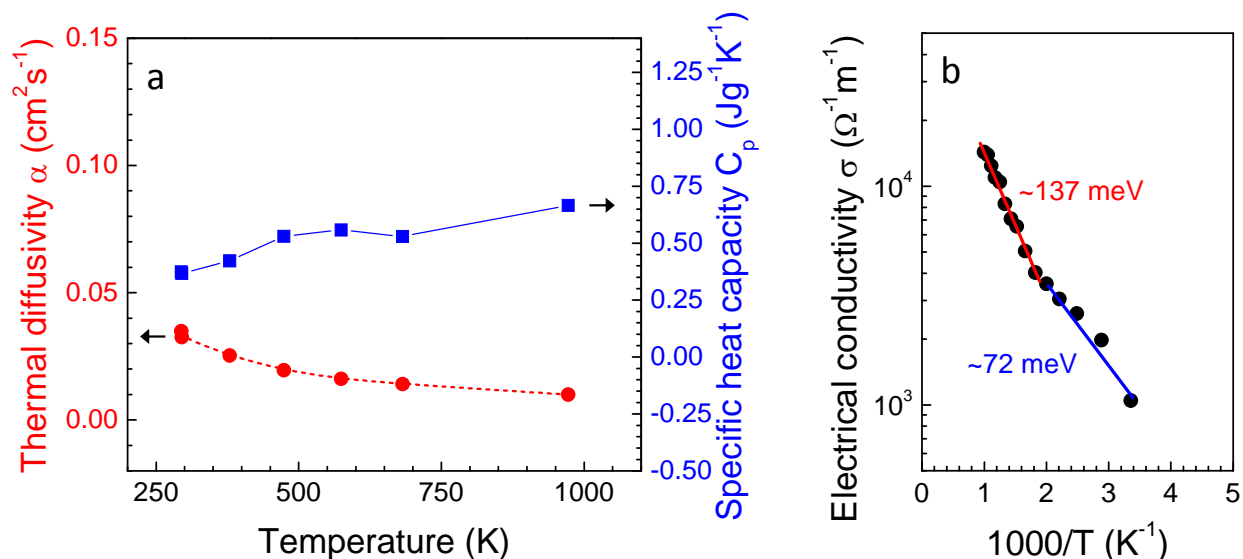R1: K. P. Ong, D. J. Singh, P. Wu, *Phys. Rev. B.* **2011**, 83, 115110.

Fig. S3. (a) Temperature-dependent thermal diffusivity and specific heat capacity, and (b) electrical conductivity versus temperature showing the two different activation energy regimes indicating the donor states for 0.5 at.% In-doped nanobulk ZnO.